PHYSICA D

Scaling laws for vortical nucleation solutions in a model of superflow

Cristián Huepe, Marc-Etienne Brachet*

Laboratoire de Physique Statistique de l'École Normale Supérieure, associé au CNRS et aux Universités Paris 6 et 7, 24 rue Lhomond, 75231 Paris Cedex 05, France

Abstract

The bifurcation diagram corresponding to stationary solutions of the nonlinear Schrödinger equation describing a superflow around a disc is numerically computed using continuation techniques. When the Mach number is varied, it is found that the stable and unstable (nucleation) branches are connected through a primary saddle-node and a secondary pitchfork bifurcation. Computations are carried out for values of the ratio ξ/d of the coherence length to the diameter of the disc in the range 1/5–1/80. It is found that the critical velocity converges for $\xi/d \to 0$ to an Eulerian value, with a scaling compatible with previous investigations. The energy barrier for nucleation solutions is found to scale as ξ^2. Dynamical solutions are studied and the frequency of supercritical vortex shedding is found to scale as the square root of the bifurcation parameter. © 2000 Elsevier Science B.V. All rights reserved.

1. Introduction

An open problem in the theory of superfluids is the determination of the critical velocity at which superfluidity breaks down [1,2]. Mathematically, at temperatures low enough for the normal component to be neglected, superfluids are described by the nonlinear Schrödinger equation (NLSE) [3,4]. Much work has been devoted to the determination of the critical velocity in this framework. The superflow around a cylinder was studied using direct simulations of NLSE by Frisch, Pomeau and Rica. They observed a transition to a dissipative regime involving vortex nucleation [5] and interpreted the results of their direct simulations in terms of a saddle-node bifurcation of the stationary solutions of the NLSE [6]. A saddle-node bifurcation was explicitly found by Hakim [7] when studying the stability of unidimensional NLSE flows across obstacles described by a potential. He obtained analytical expressions for the bifurcating stationary solutions and studied the transitional dynamics characterized by the generation of grey solitons.

---

* Corresponding author. Tel.: +33-1-44-32-37-61; fax: +33-1-44-32-34-33.
E-mail address: brachet@lps.ens.fr (M.-E. Brachet)

More recently, using numerical continuation techniques, we were able to obtain the complete bifurcation diagram corresponding to the 2D superflow around a disc [8]. It was found that the stable (elliptic) branch and the unstable (hyperbolic) branch are connected through a saddle-node bifurcation. The unstable branch generates, after a secondary pitchfork bifurcation, solutions that are asymmetric with respect to the diameter of the disc. The symmetric and asymmetric unstable solutions were found to contain, respectively, two and one vortices. Note that the flow around a cylindrical obstacle is governed by two dimensionless parameters: the Mach number $M = |\mathbf{U}|/c$ (where c is the speed of sound) associated to the flow velocity $|\mathbf{U}|$ and the ratio of the superfluid coherence length ξ to the diameter of the disc d. It turns out that ξ/d was arbitrarily fixed at $\xi/d = 1/10$ in the numerical studies reported above. It should be stressed, however, that the coherence length ξ is a microscopic length scale of the order of 1 Å in the case of superfluid ^{4}He. Note that another experimental context should be mentioned at this point: trapped Bose–Einstein condensed gases. Recent experiments were performed by moving a blue detuned laser beam through the condensate at different velocities. The ratio of the healing length to the diameter of the beam was $\xi/d \sim 1/10$ [9].

The main motivation of the present work is to study the scaling of the bifurcation diagram when ξ/d is decreased. The critical dynamics of solutions will also be studied using slightly perturbed unstable solutions as initial data. This paper is organized as follows. In Section 2, we introduce the formulation of NLSE that includes a potential used to model a disc moving in a superfluid. Our results are given in Section 3, and Section 4 is our conclusion. The appendix describes the numerical techniques used to compute the stationary and dynamical solutions of the NLSE.

2. Definition of the system

In this section, we present the hydrodynamic form of the nonlinear Schrödinger equation that models the effect of a moving disc of diameter d in a two-dimensional superfluid at rest.

We first define the following action functional:

$$\mathcal{A} = \int \mathrm{d}t \left\{ \sqrt{2}c\xi \int \mathrm{d}^2x \frac{\mathrm{i}}{2} \left(\bar{\psi} \frac{\partial \psi}{\partial t} - \psi \frac{\partial \bar{\psi}}{\partial t} \right) - \mathcal{F} \right\}, \tag{1}$$

where ψ is a complex field, $\bar{\psi}$ its conjugate and $\mathcal{F}$ is the energy of the system. We show at the end of this section that c and ξ are the physical parameters characterizing the superfluid. They correspond to the speed of sound (c) for a fluid with mean density $\rho_0 = 1$, and to the coherence length (ξ).

The energy $\mathcal{F}$ reads

$$\mathcal{F} = \mathcal{E} - \mathbf{P} \cdot \mathbf{U} \tag{2}$$

with

$$\mathcal{E} = c^2 \int \mathrm{d}^2x \left([-1 + V(\mathbf{x})]|\psi|^2 + \frac{1}{2}|\psi|^4 + \xi^2|\nabla\psi|^2 \right), \tag{3}$$

$$\mathbf{P} = \sqrt{2}c\xi \int \mathrm{d}^2x \frac{\mathrm{i}}{2} \left(\psi \nabla\bar{\psi} - \bar{\psi} \nabla\psi \right), \tag{4}$$

where the potential $V(r) = (V_0/2)(\tanh[4(r-d/2)/\Delta]-1)$ is used to represent the disc. The calculations presented below were realized with $V_0 = 10$ and $\Delta = \xi$. With these values, the fluid density inside the disc is neglectable and the density boundary layer is well resolved with a mesh adapted to the coherence length.

The Euler–Lagrange equation corresponding to (1) furnishes the following NLSE:

$$\frac{\partial \psi}{\partial t} = \frac{-i}{\sqrt{2}c\xi}\frac{\delta \mathcal{F}}{\delta \bar{\psi}} = i\frac{c}{\sqrt{2}\xi}(\Omega(\mathbf{x})\psi - |\psi|^2\psi + \xi^2\nabla^2\psi) + \mathbf{U}\cdot\nabla\psi, \tag{5}$$

where $\Omega(\mathbf{x}) = 1 - V(|\mathbf{x}|)$.

Note that the $\mathbf{U}\cdot\nabla\psi$ term in (5) could be removed by the change of variable $\mathbf{x} = \mathbf{x}' + \mathbf{U}t$. Expressed in the $\mathbf{x}'$ coordinates, the disc would be described by the potential $\Omega(\mathbf{x}) = \Omega(\mathbf{x}' + \mathbf{U}t)$ and thus be moving at a constant velocity $\mathbf{U}$. However, for convenience, we keep the $\mathbf{U}\cdot\nabla\psi$ term in (5) so that stationary solutions of (5) correspond to solutions of the NLSE equation with the disc in uniform translation in the $\mathbf{x}'$ coordinates.

The NLSE (5) can be mapped into two hydrodynamical equations by applying Madelung's transformation [2,10]:

$$\psi = \sqrt{\rho}\exp\left(\frac{i\phi}{\sqrt{2}c\xi}\right). \tag{6}$$

The real and imaginary parts of the NLSE produce for a fluid of density ρ and velocity

$$\mathbf{v} = \nabla\phi - \mathbf{U}, \tag{7}$$

the following equations of motion:

$$\frac{\partial \rho}{\partial t} + \nabla(\rho\mathbf{v}) = 0, \tag{8}$$

$$\left[\frac{\partial \phi}{\partial t} - \mathbf{U}\cdot\nabla\phi\right] + \frac{1}{2}(\nabla\phi)^2 + c^2[\rho - \Omega(\mathbf{x})] - c^2\xi^2\frac{\nabla^2\sqrt{\rho}}{\sqrt{\rho}} = 0. \tag{9}$$

In the coordinate system $\mathbf{x}$ that follows the obstacle, these equations correspond to the continuity equation and to the Bernoulli equation [1] (with a supplementary *quantum pressure* term $c^2\xi^2\nabla^2\sqrt{\rho}/\sqrt{\rho}$) for an isentropic, compressible and irrotational flow. Note that in the limit where $\xi/d \to 0$, the quantum pressure term vanishes and we recover the system of equations describing an Eulerian flow.

Using this identification, one can derive the dispersion relation for acoustic waves propagating around a constant density level $\rho = \rho_0$ as [11]:

$$\omega = \sqrt{c^2\rho_0 k^2 + \frac{\xi^2}{2}c^2k^4}. \tag{10}$$

For small wave numbers, one recovers the usual sound wave propagation. The speed of sound is uniquely defined in terms of the fluid mean density ρ_0 as

$$\lim_{k\to 0}\frac{d\omega}{dk} = c\sqrt{\rho_0}, \tag{11}$$

which justifies our definition of c as the speed of sound when $\rho_0 = 1$. For small wave number acoustic waves, the last term of (9) does not play a significant role. The length scale at which the dispersive term becomes noticeable corresponds to the coherence length ξ.

Note that there also exist vortical stationary solutions of (5) corresponding to topological defects (zeros) of the complex field ψ. Close to the centre of the vortex, the density behaves as $\rho = r^2$. The tangential velocity is given by $v = \sqrt{2}c\xi/r$, and the characteristic size of the core of the vortex is given by ξ. Thus, the velocity circulation around a vortex is given by $\Gamma = 2\pi\sqrt{2}c\xi$. For a Bose condensate of particles of mass m, the quantum of circulation has the Onsager–Feynman value $\Gamma = h/m$ (with h the Planck's constant) [11].

3. Results

We now turn to our numerical results on the properties of the stationary and dynamical solutions of (5). In Section 3.1, using the Mach number $M = |\mathbf{U}|/c$ as a control parameter, we compute the bifurcation diagrams of the stationary solutions for various values of ξ/d. In Section 3.2, we use these solutions to construct initial conditions that are well adapted to the controlled study of the dynamical evolution through time integration.

3.1. Stationary solutions

The value $\mathcal{F}(M) - \mathcal{F}(0)$ (change of the energy $\mathcal{F}$ relative to zero Mach number) found by our numerical procedure is displayed in Fig. 1 as a function of the Mach number M for various values of ξ/d. As can be seen by inspection of the figure, for each ξ/d, the stable branch (solid line) disappears with the unstable solution (dashed line) at a
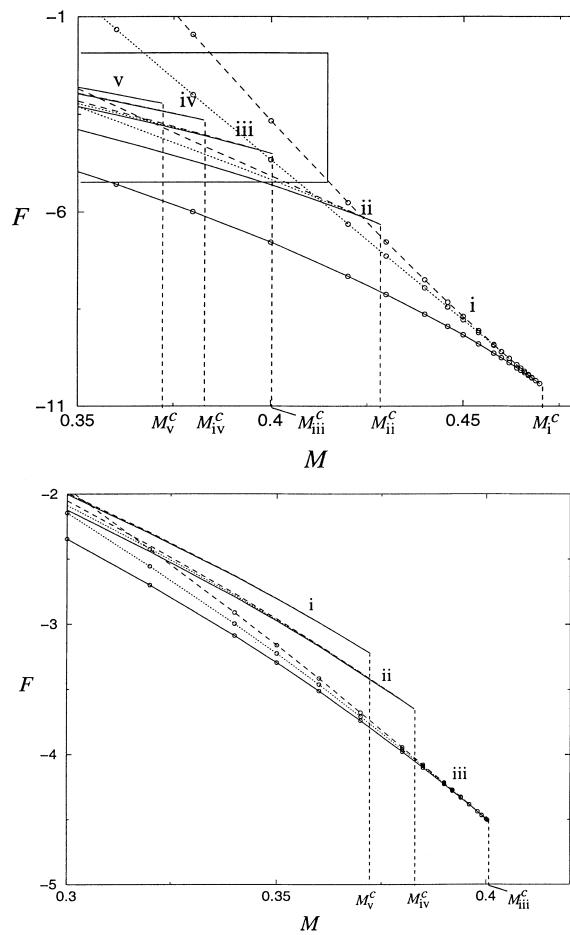

Fig. 1. Top: plots of the energy of the stationary state ($\mathcal{F}(M) - \mathcal{F}(0)$) versus Mach number ($M = |\mathbf{U}|/c$) for $\xi/d = 1/5$ (i), $\xi/d = 1/10$ (ii), $\xi/d = 1/20$ (iii), $\xi/d = 1/40$ (iv) and $\xi/d = 1/80$ (v). For each ξ/d there is a stable branch (solid line) and two unstable branches corresponding to asymmetric (dotted line) and symmetric (dashed line) solutions. The Mach values at which numerical computations were performed are marked by ($\circ$) on curves i (top) and iii (bottom) only. Bottom: blow up of the inset shown in the top figure.

saddle-node bifurcation when $M = M^c$. There are no stationary solutions beyond this point. The energy $\mathcal{F}$ has a cusp at the bifurcation point.

This qualitative behaviour is the generic signature of a Hamiltonian saddle node (HSN) bifurcation defined, at lowest order, by the normal form [12]:

$$m_{\text{eff}} \ddot{Q} = \delta - \beta Q^2, \tag{12}$$

where $\delta = (1 - M/M^c)$ is the bifurcation parameter. Here, Q is a critical amplitude and the parameters β and m_{eff} can be linked to critical scaling laws. Indeed, defining the appropriate energy

$$\mathcal{F} = \mathcal{F}_0 + m_{\text{eff}} \dot{Q}^2/2 - \delta Q + \beta Q^3/3 - \gamma \delta, \tag{13}$$
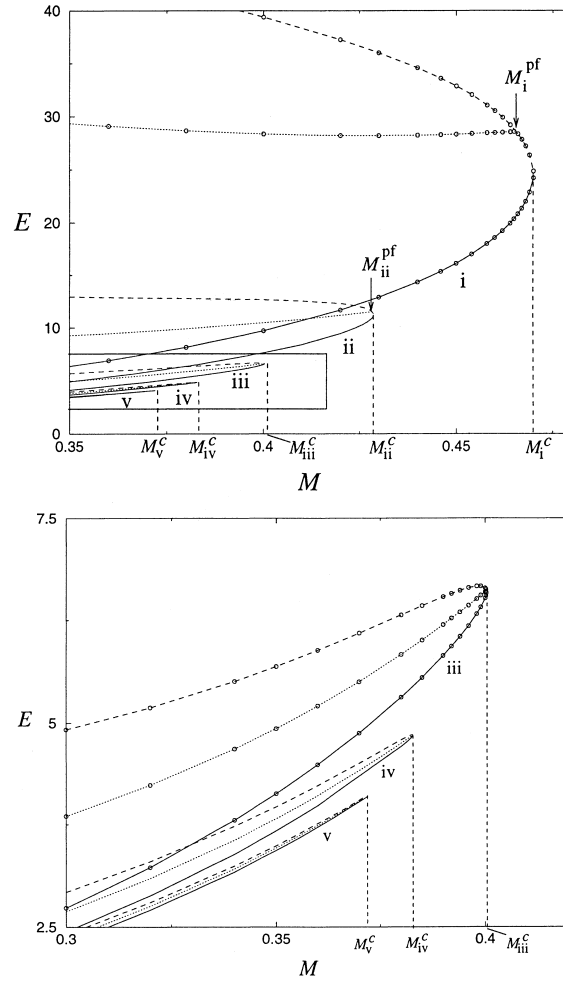

Fig. 2. Top: plots of the functional $(\mathcal{E}(M) - \mathcal{E}(0))$ versus Mach number ($M = |\mathbf{U}|/c$) for $\xi/d = 1/5$ (i), $\xi/d = 1/10$ (ii), $\xi/d = 1/20$ (iii), $\xi/d = 1/40$ (iv) and $\xi/d = 1/80$ (v). For each ξ/d there is a stable branch (solid line) and two unstable branches corresponding to asymmetric (dotted line) and symmetric (dashed line) solutions. The pitchfork bifurcation is marked by M^{pf} on curves i and ii. The Mach values at which numerical computations were performed are marked by ($\circ$) on curves i (top) and iii (bottom) only. Bottom: blow up of the inset shown in the top figure.

it is straightforward to derive from (12), close to the critical point $\delta = 0$, the universal scaling law

$$\mathcal{F}_{\pm} = \mathcal{F}_c - \mathcal{F}_1 \delta \pm \mathcal{F}_\Delta \delta^{3/2}, \tag{14}$$

where $\mathcal{F}_-$ is the energy of the stable stationary field and $\mathcal{F}_+$ is the energy of the unstable stationary field. The constants in (14) are related to those in (12) by the relations $\mathcal{F}_c = \mathcal{F}_0$, $\mathcal{F}_1 = \gamma$ and $\mathcal{F}_\Delta = 2/3\sqrt{\beta}$. Note that the $\gamma\delta$ term in (13) does not contribute to the equations of motion (12), but is responsible for the linear term in (14). The dynamical content of the HSN normal form (12) can be understood by the following considerations. The phase-space is separated into two regions by a separatrix (homoclinic orbit) that starts and ends at the hyperbolic fixed point. Trajectories inside the separatrix remain bounded near the elliptic fixed point. If the system is taken beyond the separatrix by a perturbation (e.g. thermal excitations), it will fall into unbounded (hyperbolic) trajectories. As M approaches M^c, the bounded region around the elliptic fixed point is reduced and the flow becomes more unstable. At $M = M^c$ the elliptic fixed point meets the hyperbolic fixed point and the separatrix disappears. No stationary flow can be formed for $M > M^c$. Note that the appropriate normal form is Hamiltonian because (5) is invariant under the following time reversal transformation:

$$t \to -t, \quad \psi \to \psi^*, \quad x \to -x. \tag{15}$$

At $M = M^{pf}$ (see Fig. 2), the unstable symmetric branch (dashed line) bifurcates at a pitchfork to a pair of asymmetric branches (dotted line) [8]. It can be directly checked on our results (see Fig. 3 below) that the secondary pitchfork bifurcation breaks the $y \to -y$ symmetry of the flow.
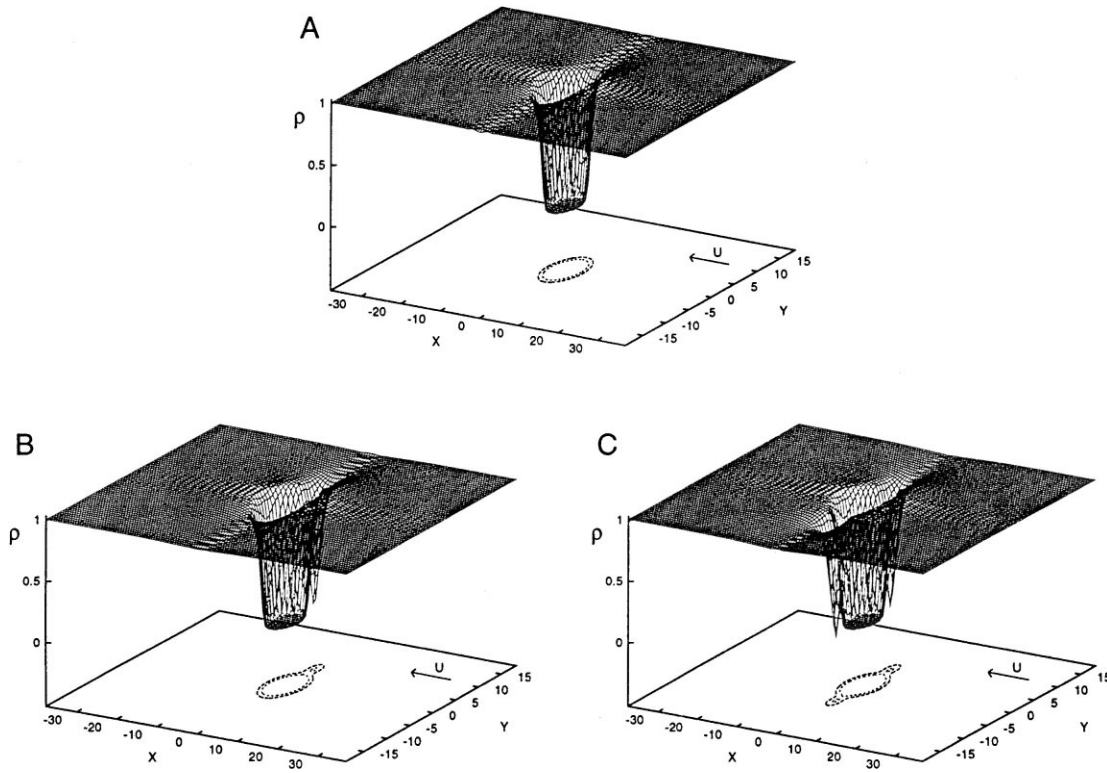

Fig. 3. Stationary states for $M = 0.24$ and $\xi/d = 1/10$: stable (A), one vortex unstable (B), two vortices unstable (C). The surface indicates the fluid density ρ around the cylinder.
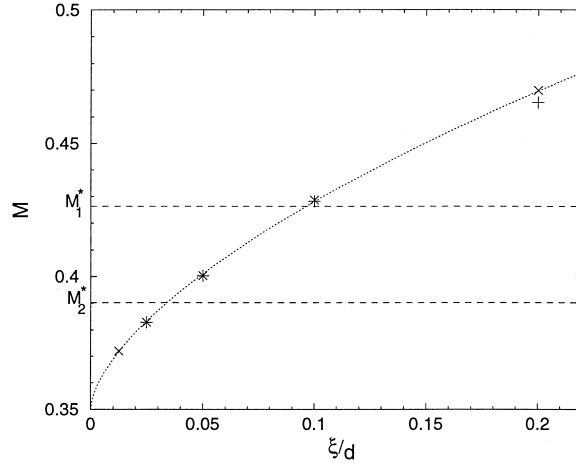
Fig. 4. Saddle-node bifurcation Mach number M^c (×) and pitchfork bifurcation Mach number M^{pf} (+) as a function of ξ/d. The dotted curve corresponds to a fit to the polynomial law $M^c = K_1(\xi/d)^{K_2} + M^c_{Euler}$ with $K_1 = 0.322$, $K_2 = 0.615$ and $M^c_{Euler} = 0.35$. The dashed lines $M^*_1 \approx 0.4264$ and $M^*_2 \approx 0.3903$ correspond, respectively, to first-and-second-order compressible corrections to the $M^c = 0.5$ critical velocity computed using a local sonic criterion for an incompressible flow (see text). Note that the agreement, that is claimed to exist in [5,6], between the $\xi/d = 1/10$ numerical result and M^*_1 is shown to be spurious.

In Fig. 2, the bifurcation diagrams are presented in the same conditions as those of Fig. 1, but for the functional $\mathcal{E}(M) - \mathcal{E}(0)$ (change of $\mathcal{E}$ relative to zero Mach number) as a function of M. The pitchfork bifurcation is marked by M^{pf} in the $\xi/d = 1/5$ and $\xi/d = 1/10$ case. For smaller values of ξ/d, the pitchfork and the saddle-node Mach numbers can no longer be resolved.

From Figs. 1 and 2, it is apparent that as $\xi/d \to 0$, the three branches approach each other and the pitchfork gets closer to the saddle-node. This behaviour is compatible with an Eulerian flow limit for $\xi/d = 0$.

By visualizing the stationary solutions of the NLSE we can relate the branches of Figs. 1 and 2 to the presence of vortices. Fig. 3 shows the density $\rho = |\psi|^2$ of typical stationary solutions for $M = 0.24$ and $\xi/d = 1/10$. It is apparent by inspection of the figure that the stable branch is irrotational (Fig. 3A) while the unstable branch (B) corresponds to a one vortex solution, and the unstable branch (C) to a two vortex solution. As M is increased, the distance between the vortices and the obstacle on the unstable branches (Fig. 3B and C) decreases. At a certain $M < M^c$, they disappear on the surface on the cylinder, generating an irrotational flow. See [8] for a detailed study of the Mach number at which the vortex emerges from the disc.

We now study the dependence of ξ/d on the main features of the bifurcation diagram. In Fig. 4 the saddle-node Mach number M^c (crosses) and the pitchfork Mach number M^{pf} (pluses) are displayed as a function of ξ/d. As we have already pointed out, when ξ/d is decreased, M^c and M^{pf} become indistinguishable. In the limit where $\xi/d = 0$, the critical Mach number M^c will be that of an Eulerian flow M^c_{Euler}.

This convergence to the Eulerian critical velocity can be characterized by fitting the polynomial law $M^c = K_1(\xi/d)^{K_2} + M^c_{Euler}$ to the M^c results. The dotted line in Fig. 4 shows such a fit yielding $K_1 = 0.322$, $K_2 = 0.615$ and $M^c_{Euler} = 0.35$. This result is compatible with the analytical approximate results presented in [13,14] that predicts a square root ($K_2 = 0.5$) polynomial dependence on ξ/d.

The dashed line M^*_1 in Fig. 4 corresponds to the critical velocity $M^c = \sqrt{2/11}$ obtained in [5] by applying a local sonic criterion through the following procedure. Neglecting the quantum pressure term, the continuity (8) and Bernoulli (9) equations for a stationary flow become

$$\nabla \cdot (\rho \nabla \phi') = 0, \tag{16}$$

$$c^2(\rho - \rho_\infty) = \frac{|\mathbf{U}|^2}{2} - \frac{(\nabla\phi')^2}{2},$$

(17)

where a new phase variable $\phi' = \phi - \mathbf{U}x$ has been defined so that the local velocity can be expressed as $\mathbf{v} = \nabla\phi'$ (see Eq. (7)). This system together with the appropriate boundary conditions $\lim_{x\to\infty}\phi' = -\mathbf{U}$ and $\nabla_{\hat{n}}\phi' = 0$ (where $\nabla_{\hat{n}}$ stands for the derivative of ϕ' in the direction perpendicular to the surface of the disc) can be solved by an iterative scheme.

The first step consists in considering the density constant. The continuity equation is then simply a harmonic equation for the phase. Its solution satisfying the corresponding boundary conditions is readily found to be [1]:

$$\phi'_0 = -|\mathbf{U}|\cos(\theta)\left[r + \frac{(d/2)^2}{r}\right],$$

(18)

where r and θ are the standard polar coordinates with origin at the centre of the disc. This solution corresponds to a flow velocity field $\mathbf{v} = \nabla\phi'_0$ with maximums located at $\theta = \pm\pi/2$ and equal to $2|\mathbf{U}|$. Introducing ϕ'_0 into the Bernoulli equation (17) gives the first correction to the local density ρ. The local sound speed can then be computed using Eq. (11): $c = \sqrt{\rho}$. By supposing that the stationary solutions disappear when the local velocity is larger than the local speed of sound (Landau's sonic criterion) it is then straightforward to obtain a first-order approximation to the saddle-node Mach number as $M_1^* = \sqrt{2/11} \approx 0.4264$ [5].

This approximation for the critical velocity can be improved by another iteration. Solving the continuity equation with the corrected value of the density ρ yields an improved solution for ϕ'. Applying the local sonic criterion for this new velocity field one obtains the next order approximation [15] to the critical Mach number $M_2^* = \sqrt{\sqrt{233} - 11}/(2\sqrt{7}) \approx 0.3903$.

Note that it is apparent in Fig. 4 that the agreement that is claimed to exist in [5] between the $\xi/d = 1/10$ numerical computations and the first-order critical velocity approximation M_1^* is a mere coincidence. Our present
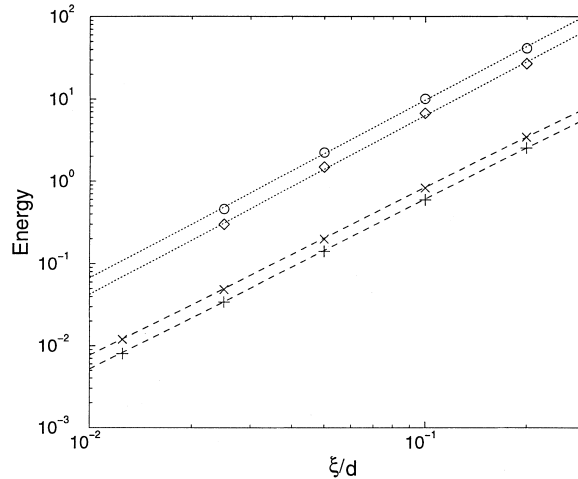

Fig. 5. Energy gap between branches as a function of ξ/d. The ($\times$) and ($+$) show the difference between the energy $\mathcal{F}$ of the one-vortex unstable solution and the stable solution for Mach numbers $M = M_{\xi/d}^c - 0.1$ ($\times$) and $M = M_{\xi/d}^c - 0.08$ ($+$) (where $M_{\xi/d}^c$ is the critical Mach number as a function of ξ/d). The dashed lines correspond to the polynomial fits $\Delta\mathcal{F} = 92.2(\xi/d)^{2.04}$ for ($\times$) and $\Delta\mathcal{F} = 71.5(\xi/d)^{2.07}$ for ($+$). The circles and the diamonds show the saddle-node amplitudes $A_{\mathcal{F}}$ and $A_{\mathcal{E}}$ for $\mathcal{F}$ and $\mathcal{E}$, respectively (see text). The solid lines show the fits given by $A_{\mathcal{E}} = 1406(\xi/d)^{2.16}$ and $A_{\mathcal{F}} = 932(\xi/d)^{2.17}$.

results, based on the $\xi/d \to 0$ solutions of the NLSE, point to a limit velocity of about $M_{\text{Euler}}^{\text{c}} = 0.35$. We have been unable to find in the literature a computation of the precise value of $M_{\text{Euler}}^{\text{c}}$. The problem of its direct determination, starting from the Euler equation, is left for future work.

Fig. 5 shows the variation with ξ/d of the gap between the stable and unstable energy branches (see Figs. 1 and 2). At the tip of the bifurcation, we characterize this gap as a function of ξ/d by using two quantities. The circles indicate the saddle-node amplitude $\Delta\mathcal{F} = 2\mathcal{F}_\Delta$ (see Eq. (14)), and the diamonds present the saddle-node amplitude $\Delta\mathcal{E} = 2\mathcal{E}_\Delta$ corresponding to the scaling law for the functional $\mathcal{E}$: $\mathcal{E}_+ - \mathcal{E}_- = \mathcal{E}_\Delta \delta^{1/2}$. The gap is also characterized, at a finite distance from the tip of the bifurcation, as the $\mathcal{F}$ energy difference between the one-vortex unstable solution and the stable solution at Mach numbers $M = M_{\xi/d}^{\text{c}} - 0.1$ (indicated by crosses) and $M = M_{\xi/d}^{\text{c}} - 0.08$ (indicated by pluses), where the vortices are well detached from the cylinder. Here, $M_{\xi/d}^{\text{c}}$ is the critical Mach number of the corresponding ξ/d.

The data shown in Fig. 5 shows that our numerical results follow a $(\xi/d)^2$ scaling. Note that this scaling law was proposed in [6] based on the existence of detached vortices. It is therefore not surprising that it applies to the
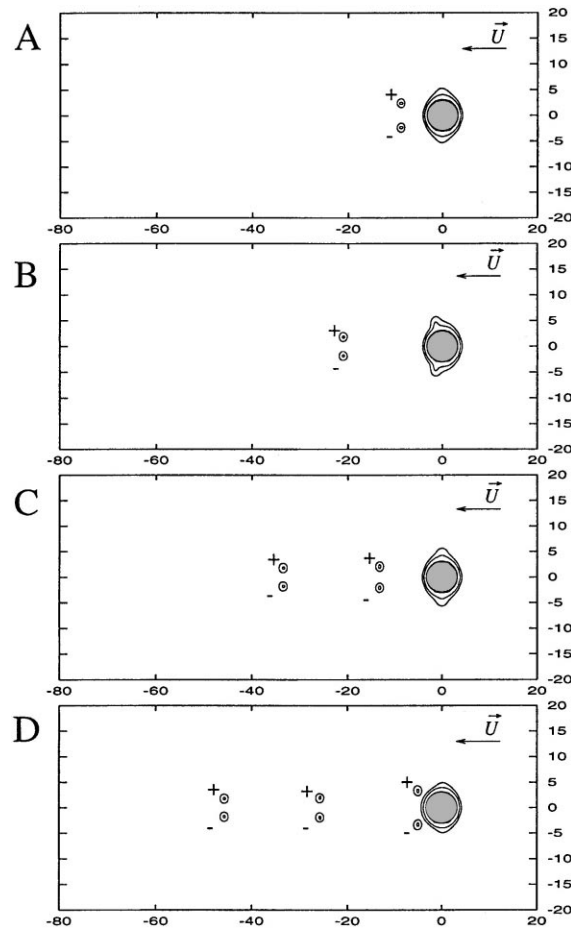

Fig. 6. Evolution of the NLSE time integration at a supercritical Mach number $M^{\text{c}} = 0.9$ starting from a *symmetric* (two vortices) unstable stationary solution at $M = 0.7$. Here, $\xi/d = 1/20$ and $M^{\text{c}} \approx 0.382$. The images correspond to $t = 1 \times 10^4$ (A), $t = 2 \times 10^4$ (B), $t = 3 \times 10^4$ (C), $t = 4 \times 10^4$ (D) in natural (ξ/c) time units. A clearly defined periodicity on the emission of $+$ and $-$ vortex pairs appears.

energy gap between the one-vortex unstable solution and the stable solution. Our results further demonstrate that the $(\xi/d)^2$ scaling also applies to the bifurcation amplitudes $A_{\mathcal{F}}$ and $A_{\mathcal{E}}$.

3.2. Dynamical solutions

The stationary solutions obtained above provide us with adequate initial data for the study of dynamical solutions. Indeed, after a small perturbation, their integration in time will generate a dynamical evolution with very small acoustic emission. This procedure also provides an efficient way to start vortical dynamics in a controlled manner.

Figs. 6 and 7 show the evolution of the NLSE time integration at a supercritical Mach number $M^c = 0.9$ that is obtained starting, respectively, from a two-vortex and one-vortex unstable stationary solution. While Fig. 6 displays a clearly defined periodicity on the emission of $+$ and $-$ vortex pairs, Fig. 7 shows a disorganized wake. Indeed, initial condition given by the one-vortex unstable stationary solution is essentially different from the two-vortex
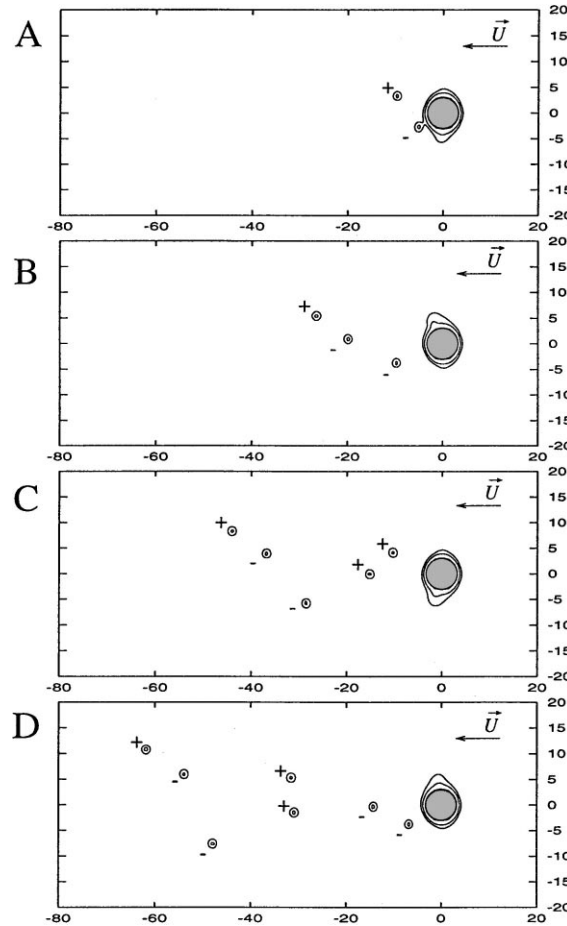

Fig. 7. Evolution of the NLSE time integration, at a supercritical Mach number $M^c = 0.9$ starting from a *nonsymmetric* (one vortex) unstable stationary solution at $M = 0.7$. Here, $\xi/d = 1/20$ and $M^c \approx 0.382$. The images correspond to the same times as in Fig. 6. Since this initial condition presents a nonzero circulation around the cylinder (in contrast with the two-vortex unstable initial condition shown in Fig. 6), the perturbation of this solution produces a peculiar pattern of vortex emission: $+, -, -, +, +, -, -, +, +$, etc. The circulation around the cylinder oscillates symmetrically about 0. The resulting wake is extremely disorganized, in sharp contrast with Fig. 6.
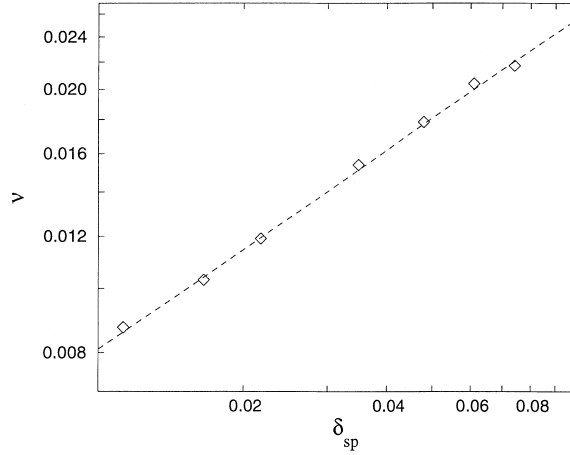
Fig. 8. Vortex emission frequency as a function of $\delta_{sp} = (M - M^c)/M^c \ll 1$ (with $M^c = 0.3817$) for a symmetric wake (as in Fig. 7) and $\xi/d = 1/20$. The dashed line shows a fit of a polynomial $\nu = K_1 \delta_{sp}^{1/2}$ with $K_1 = 0.081$. The obtained $\delta_{sp}^{1/2}$ law for the frequency is equivalent to the one expected for a dissipative system.

one since it presents a nonzero circulation around the cylinder. This characteristic forces the emission of a second (oppositely charged) vortex in order for the disc to have a zero circulation as the first vortex is dragged to infinity. This pattern is followed by the emission of a second oppositely charged vortex. The system then goes through the peculiar pattern of vortex emission given by $+, -, -, +, +, -, -, +, +$, etc. The circulation around the cylinder therefore oscillates symmetrically about 0.

In order to study the behaviour of the frequency of vortex emission close to the bifurcation, we have measured it in the symmetrical wake corresponding to Fig. 6 for several supercritical velocities (characterized by $\delta_{sp} = -\delta > 0$). Our results, plotted in Fig. 8, are consistent with a $\delta_{sp}^{1/2}$ scaling, which is unexpected in a Hamiltonian system.

The Andronov saddle-node and homoclinic bifurcations [16] have been shown recently to be relevant for the study of dissipative extended systems [17,18]. The simple case of the saddle-node Andronov bifurcation is produced when there exists an homoclinic connection at the bifurcation point. The homoclinic orbit generates a limit cycle whose period diverges at the bifurcation with the timescale τ of evolution near the bifurcation point. In the case of dissipative systems whose saddle-node bifurcation is controlled by the normal form

$$m_{\text{eff}} \dot{Q} = \delta - \beta Q^2, \tag{19}$$

the timescale is found to be $\tau \sim \delta_{sp}^{-1/2}$ by a simple scaling argument.

If the Hamiltonian normal form (12) is used instead of (19), the timescale τ is given by $\tau \sim \delta_{sp}^{-1/4}$. Thus, in contradiction with the results presented in Fig. 8, the frequency should diverge as $\nu \sim \delta_{sp}^{1/4}$. The relevance of the dissipative scaling to our numerical results can perhaps be understood by the following physical arguments. The system is generating vortices that are carried away by the flow. It behaves in a dissipative way because the incident kinetic energy of the flow is irreversibly transferred to the vortical wake. Indeed, a time reversal of the type defined in (15) will transform the system into a highly nongeneric state that requires a very special preparation of the system. However, the proper extension to infinite nondissipative systems (such as the one studied in the present paper) of the dissipative system results such as those given in [17,18] remains to be done.

Note that Josserand et al. [14] have derived a more complex equation than the normal form (19) in an approach that uses the Euler–Tricomi equation supplemented by suitable asymptotic corrections. This equation reads

$$\ddot{Q} + \mathrm{i}\omega\dot{Q} = \delta - Q^2. \tag{20}$$

This expression is time reversible and its stationary solutions correspond to a purely real Q. A formal argument using the oscillating term $\dot{Q}$ would give the scaling $\nu \sim \delta^{1/2}$ close to $\delta = 0$. However, the instability in (20) can be shown to be a Hopf bifurcation occurring at $\delta = \omega^4/64$ with a finite frequency.

Our results were obtained in a close vicinity of M^c ($\delta_{sp} < 0.1$). Note that in a much larger range $\delta_{sp} \sim 1$, it was reported in [5] that a linear scaling on δ seems to be followed by the vortex emission frequency. This result is not incompatible with our result because of the different range of δ in which they, respectively, apply.

4. Conclusion

The main results presented in this paper are the scaling laws that characterize the dependence of ξ/d on the bifurcation diagram for stationary solutions of the NLSE. The critical Mach number M^c, at which the stationary stable and stationary unstable solutions meet in a saddle-node bifurcation was found to tend to the Eulerian critical Mach number $M^c_{Euler} \approx 0.35$, following a $M^c - M^c_{Euler} \propto (\xi/d)^{0.615}$ law. This result is compatible with the $M^c - M^c_{Euler} \propto (\xi/d)^{1/2}$ dependence predicted in [13,14]. The dependence of ξ/d on the energy gap between the stable and unstable stationary solution (nucleation barrier) was studied near and far from the tip of the saddle-node bifurcation. The bifurcation amplitude and the energy difference between the one-vortex unstable and the stable branches at a given Mach number show that this nucleation energy barrier vanishes as $(\xi/d)^2$.

Using slightly perturbed stationary solutions as initial conditions, the dynamics of solutions beyond the saddle-node bifurcation was also studied. While a perturbed symmetric unstable stationary solution was found to generate a periodic vortex wake, a nonsymmetric solution produces a disorganized wake by generating vortices that follow the emission pattern $+, -, -, +, +, -, -, +, +$, etc. The symmetric wake frequency was measured as a function of the supercritical velocity parameter. The resulting scaling law was surprisingly found to correspond to the one of dissipative systems.

Acknowledgements

Appendix A. Numerical methods

In this appendix, we describe the numerical techniques used to compute the stationary and dynamical solutions of Eq. (5).

Eq. (5) follows a conservative dynamics, and therefore does not relax towards a minimum of the energy $\mathcal{F}$. Nevertheless, the stable stationary states of (5) corresponding to a minimal $\mathcal{F}$ can be reached by integrating forward the real Ginzburg–Landau equation (RGLE) associated to (5)

$$\frac{\partial \psi}{\partial t} = -\frac{1}{\sqrt{2}c\xi}\frac{\delta F}{\delta \bar{\psi}} = \frac{c}{\sqrt{2}\xi}(\Omega(\mathbf{x})\psi - |\psi|^2\psi + \xi^2\nabla^2\psi) - i\mathbf{U}\cdot\nabla\psi. \tag{A.1}$$

Indeed, (5) and (A.1) have the same stationary solutions. Eq. (A.1) is integrated to convergence by using the Forward-Euler/Backwards-Euler time stepping scheme

$$\psi(t+\sigma) = \Theta^{-1}\left[(1 - i\sigma\mathbf{U}\cdot\nabla)\,\psi(t) + \sigma\frac{c}{\sqrt{2}\xi}(\Omega(\mathbf{x})\psi(t) - |\psi(t)|^2\psi(t))\right], \tag{A.2}$$

where

$$\Theta = \left[1 - \sigma \frac{c\xi}{\sqrt{2}} \nabla^2 \right]. \tag{A.3}$$

The advantage of this time stepping method is that it converges to the stationary solution of (5) independent of the time step σ.

We use Newton's method [19] to find unstable stationary solutions of the RGLE. In order to work with a well-conditioned system [20], we search for fixed points of (A.2). Calling $\psi_{(j)}$ the value of the field ψ over the jth collocation point, this is equivalent to finding ψ^* such that

$$f_{(j)}(\psi^*) \equiv \psi^*_{(j)}(t + \sigma) - \psi^*_{(j)}(t) = 0. \tag{A.4}$$

Every Newton step thus requires the solution for $\delta\psi_{(k)}$ of

$$\sum_k \left[\frac{\mathrm{d}f_{(j)}}{\mathrm{d}\psi_{(k)}} \right] \delta\psi_{(k)} = -f_{(j)}(\psi), \tag{A.5}$$

which is done by an iterative bi-conjugate gradient method (BCGM) [21]. This method uses the direct application of $[\mathrm{d}f_{(j)}/\mathrm{d}\psi_{(k)}]$ over an arbitrary field φ, given by

$$\sum_k \left[\frac{\mathrm{d}f_{(j)}}{\mathrm{d}\psi_{(k)}} \right] \varphi_{(k)} = \left\{ \Theta^{-1} \left[(1 - \mathrm{i}\sigma \mathbf{U} \cdot \nabla) \varphi + \sigma \frac{c}{\sqrt{2}\xi} (\Omega(|x|)\varphi - \psi^2 \bar{\varphi} - 2|\psi|^2 \varphi) \right] - \varphi \right\}_{(j)}.$$

Since the convergence of the time step (A.2) does not depend on σ, the roots found through this Newton iteration are also independent of σ. Therefore, σ becomes a free parameter that can be used to adjust the preconditioning of the system in order to optimize the convergence of the BCGM [20].

We use standard Fourier pseudo spectral methods [22]. Typical convergences of the Newton and bi-conjugate gradient iterations are shown in Figs. 9 and 10. The computer resources needed to generate the bifurcation diagrams presented below on a CRAY C90 are summarized in Table 1.
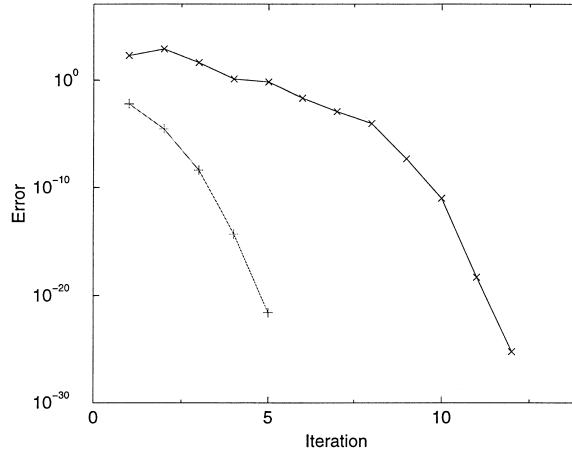

Fig. 9. Two typical examples of the Newton method convergence towards the solution of Eq. (A.4) for $\xi/d = 1/10$ and a field $\psi_{(j)}$ discretized into $n = 128 \times 64 = 8190$ collocation points. The error measure is given by $\sum_{j=1}^{n} f_{(j)}^2(\psi)/n$. The convergence is faster than exponential, as expected for a Newton method.
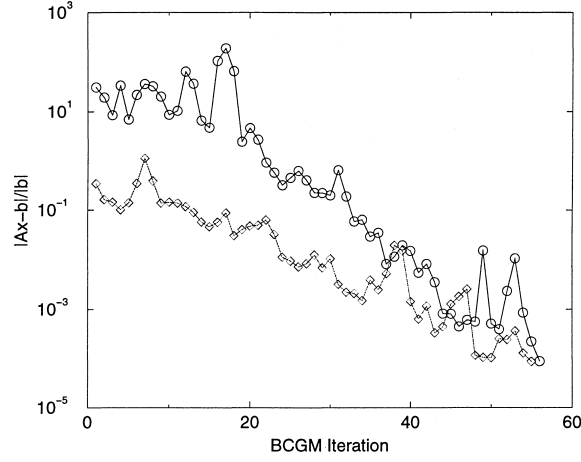
Fig. 10. Two typical examples of a bi-conjugate gradient method convergence corresponding to the case shown in Fig. 9. The convergence of the relative error in the **x** solution of **Ax**=**b** is given by $|\mathbf{Ax} - \mathbf{b}|/|\mathbf{b}|$, where $\mathbf{A} = [\mathrm{d}f_{(j)}/\mathrm{d}\psi_{(k)}]$, $\mathbf{b} = -f_{(j)}(\psi)$ and $\mathbf{x} = \delta\psi_{(k)}$ (see Eq. (A.5)).

Note that it is possible to reduce the precision required for the BCGM routine down to $\sim 10^{-1}$. In this case, the convergence of (A.5) becomes simply exponential. Such a quasi-Newton scheme was used for $\xi/d \leq 1/40$.

The time integration of the NLSE is done by using a fractional step (Operator-Splitting) method [23]. We construct an exponential operator generating a forward time evolution. We divide this operator into one part that is computed in spectral space

$$\mathcal{T}_{\mathrm{L}}(\mathbf{k}, \Delta t) = \exp\left[\mathrm{i}\left(\frac{c}{\sqrt{2}\xi} + \mathbf{U} \cdot \mathbf{k} - \mathbf{k}^2\right)\Delta t\right], \tag{A.6}$$

and another part that is computed in physical space

$$\mathcal{T}_{\mathrm{NL}}(\mathbf{x}, \Delta t) = \exp\left[-\mathrm{i}\left(V(\mathbf{x}) + \frac{c}{\sqrt{2}\xi}|\psi(\mathbf{x}, t)|^2\right)\Delta t\right]. \tag{A.7}$$

The time step is then given by

$$\hat{\psi}(\mathbf{k}, t + \Delta t) = \mathcal{T}_{\mathrm{L}}(\mathbf{k}, \Delta t/2)\mathcal{F}\left[\mathcal{T}_{\mathrm{NL}}(\mathbf{x}, \Delta t)\mathcal{F}^{-1}[\mathcal{T}_{\mathrm{L}}(\mathbf{k}, \Delta t/2)\hat{\psi}(\mathbf{k}, t)]\right], \tag{A.8}$$

where $\mathcal{F}$ and $\mathcal{F}^{-1}$ represent the direct and inverse Fourier transforms, respectively.

Table 1

ξ/d	Resolution	Time
1/5	64×32	5 min
1/10	128×64	30 min
1/20	256×128	2 h
1/40	512×256	10 h
1/80	1024×512	50 h

References

[1] L. Landau, E. Lifschitz, Mécanique des Fluides, Vol. 6, Editions Mir, 1989.

[2] R.J. Donnelly, Quantized Vortices in Helium II, Cambridge University Press, Cambridge, 1991.

[3] E.P. Gross, Hydrodynamics of a superfluid condensate, J. Math. Phys. 4 (1963) 195.

[4] V.L. Ginzburg, L.P. Pitaevskii, On the theory of superfluidity, Soviet Phys. JETP 34 (7) (1958) 858.

[5] T. Frisch, Y. Pomeau, S. Rica, Transition to dissipation in a model of superflow, Phys. Rev. Lett. 69 (1992) 1644.

[6] Y. Pomeau, S. Rica, Vitesse limite et nucléation dans un modèle de superfluide, Comptes Rendus Acad. Sci. (Paris), Série II 316 (1993) 1523.

[7] V. Hakim, Nonlinear Schrödinger flow past an obstacle in one dimension, Phys. Rev. E 55 (3) (1997) 2835.

[8] C. Huepe, M.-E. Brachet, Solutions de nucléation tourbillonnaires dans un modèle d'écoulement superfluide, C.R. Acad. Sci. Paris 325 (II) (1997) 195–202.

[9] C. Raman, M. Köhl, R. Onofrio, D.S. Durfee, C.E. Kuklewicz, Z. Hadzibabic, W. Ketterle, Evidence for a critical velocity in a Bose–Einstein condensed gas, Phys. Rev. Lett. 83 (13) (1999) 2502.

[10] E.A. Spiegel, Fluid dynamical form of the linear and nonlinear schrödinger equations, Physica D 1 (1980) 236.

[11] C. Nore, M. Abid, M. Brachet, Decaying kolmogorov turbulence in a model of superflow, Phys. Fluids 9 (9) (1997) 2644.

[12] J. Guckenheimer, P. Holmes, Nonlinear Oscillations, Dynamical Systems and Bifurcations of Vector Fields. Springer, Berlin, 1983.

[13] C. Josserand, Dynamique des superfluides: Nucléation de vortex et transition de phase du permier ordre, Ph.D. Thesis, Ecole Normale Supeérieure, 1997.

[14] C. Josserand, Y. Pomeau, S. Rica, Vortex shedding in a model of superflow, Physica D 134 (1) (1999) 111–125.

[15] V. Hakim, private communication.

[16] A. Andronov, Sobraniye Trudov A.A. Andronov, Izv. A.N. SSSR, 1956.

[17] M. Argentina, Dynamique des systèmes bistables spatialement étendus, Ph.D. Thesis, Université de Nice-Sophia Antipolis, 1999.

[18] M. Argentina, P. Coullet, L. Mahadevan, Colliding waves in a model excitable medium: Preservation, annihilation, and bifurcation, Phys. Rev. Lett. 79 (15) (1997) 2803.

[19] R. Seydel, From Equilibrium to Chaos: Practical Bifurcation and Stability Analysis, Elsevier, New York, 1988.

[20] C. Mamun, L. Tuckerman, Asymmetry and Hopf bifurcation in spherical couette flow, Phys. Fluids 7 (1) (1995) 80.

[21] W. Press, S. Teukolsky, W. Vetterling, B. Flannery, Numerical Recipes in Fortran, Cambridge University Press, Cambridge, 1994.

[22] D. Gottlieb, S.A. Orszag, Numerical Analysis of Spectral Methods, SIAM, Philadelphia, PA, 1977.

[23] R. Klein, A.J. Majda, Self-stretching of perturbed vortex filaments, Physica D 53 (1991) 267.